RSC Advances

PAPER

View Article Online
View Journal | View Issue

Cite this: *RSC Adv.*, 2026, **16**, 8356

Tunable dispersion of cobalt oxide nanoclusters grafted on mesoporous SBA-15 for efficient pharmaceutical removal from wastewater

Hajar Tallouzt,[ab] Céline Nayral,[c] Jamal El Haskouri,[d] Khalil Anis,[a] Abdelhak Kherbeche[a] and Abdelkrim El Kadib *[be]

Pharmaceutical contaminants are an emerging threat, driving antibiotic resistance and environmental risk. Here, we harness the high surface area and tunable chemistry of mesoporous **SBA-15** silica to engineer hybrid adsorbents by confining ultra-small metal oxide clusters (<1 nm; NiO: 0.47 ± 0.15 nm, Co_3O_4: 0.63 ± 0.17 nm, Fe_2O_3: 0.73 ± 0.18 nm) within its mesostructured network. Consistent with its strong Lewis acidity, cobalt oxide-loaded **SBA-15** exhibited exceptional tetracycline removal efficiency, outperforming pristine **SBA-15**, aminopropyl/mercaptopropyl-functionalized silicas, bulk cobalt oxide, and other nanomaterials. Through benchmarking and accurate comparison, several key points can be made: (i) residual pluronic was pivotal for stabilizing the burst and keeping the metallic phase well dispersed and with an ultra-small size, which consequently enabled the retention of the mesostructure, (ii) thermal annealing treatment was essential for strengthening the interfacial grafting and for structural integrity, (iii) surface polarity imparted by terminal hydroxyl groups promoted strong interaction with the pharmaceutical pollutant. The photoactivatable Co–O–Si sites, reached through atomic cobalt dispersion on the silica matrix, provide an additional means for photo-oxidation, enabling near-complete degradation of highly concentrated tetracycline (10^{-3} mol L^{-1}) under visible light. Mechanistic studies reveal the involvement of hole-mediated surface reactions in the photo-triggered degradation pathway. This multifunctional, cobalt oxide decorated mesostructured **SBA-15**-type silica hybrid offers a promising platform for advanced water purification technologies.

Received 23rd October 2025
Accepted 4th February 2026

DOI: 10.1039/d5ra08136j

rsc.li/rsc-advances

Introduction

Beyond conventional pollutants such as dye effluents from the textile industry and heavy metals from mining activities, aquatic ecosystems are increasingly threatened by pharmaceutical and drug micro-pollutants, one of the most pressing environmental challenges of our time.[1–3] Pharmaceutical residues constitute a significant portion of contaminants entering wastewater treatment plants (WWTPs). Their sources are diverse, including industrial discharges, hospital effluents (notably those containing anti-cancer agents), intensive livestock farming (a major consumer of antibiotics and growth promoters), and domestic wastewater *via* human excreta.[4–6] Conventional WWTPs have proven largely ineffective in removing these residues, resulting in the contamination of surface water, groundwater, and even drinking water supplies. Among the most commonly detected compounds are anti-inflammatory drugs, antidepressants, and antibiotics.[7,8] The spread of antibiotic resistance, a natural evolutionary response to antimicrobial exposure, is accelerated by the persistent presence of such residues in the environment.[9] Even at trace concentrations, antibiotics can disrupt ecosystems and pose severe risks to human health. Tetracycline (TC), widely used in both human and veterinary medicine, is one of the most prevalent antibiotic contaminants found in nature.[10,11]

Numerous advanced treatment strategies have been explored for tetracycline removal from surface waters and WWTP effluents, including advanced oxidation processes (photolysis, ozonation, catalytic/UV degradation), membrane filtration, reverse osmosis, and adsorption.[12] Among these, adsorption stands out as one of the most efficient and scalable techniques for treating water contaminated with pharmaceutical residues.[13–16] The performance of an adsorbent strongly depends on its intrinsic properties, mainly its abundance, cost-effectiveness, textural characteristics, chemical stability, and ease of regeneration.[17] An ideal support should offer high tunability in both texture and surface chemistry, enabling broad applicability across various pollutants.

[a]*Laboratory of Materials, Process, Catalysis, Agri-food and Environment, Higher School of Technology, Sidi Mohamed Ben Abdellah University, Fez, Morocco*

[b]*Euro-Med University of Fes (UEMF), Fès, Morocco. E-mail: a.elkadib@ueuromed.org*

[c]*Laboratoire de Physique et Chimie des Nano-Objets, Université de Toulouse, CNRS, INSA, UPS, Toulouse CEDEX-4 31077, France*

[d]*Instituto de Ciènca de los Materials de la Universidad de Valencia, Calle catedratico Jose' Beltran, 2 CP 46980, Paterna, Valencia, Spain*

[e]*Hassan II Academy of Science and Technology, Rabat, Morocco*

Ordered mesoporous silica, particularly **SBA-15**, meets many of these criteria due to its high surface area, tunable pore size, large pore volume, thicker wall framework, hierarchical architecture, and straightforward surface functionalization.[18] While organically functionalized **SBA-15** materials have demonstrated promise in the subject, challenges remain, including the instability of surface tethers under harsh conditions (*e.g.*, acidic effluents) and limited efficiency toward certain neutral and more recalcitrant pharmaceuticals. Surprisingly, little attention has been given to the incorporation of nanosized metal (oxide) species into mesoporous silica for this purpose, despite their proven success in heterogeneous catalysis where efficient reactant diffusion occurs within mesopores. Analogously, such materials could be engineered to adsorb complex pharmaceutical pollutants. Moreover, many transition-metal clusters exhibit photocatalytic activity under light irradiation, offering a unique opportunity to integrate adsorption with photocatalysis in a single platform.[19] In this work, we report the synthesis of high-surface-area adsorbent–photocatalyst hybrids by impregnating mesoporous **SBA-15** with cobalt, nickel, and iron precursors. The resulting materials were thoroughly characterized in terms of chemical composition, textural features, and interfacial properties. Their performance in tetracycline removal from aqueous solutions was evaluated through kinetic and isotherm studies, with particular attention to the influence of metal loading and pH. Finally, we explored their photocatalytic activity under visible light to enhance removal efficiency and assessed material stability and recyclability for sustainable water-cleaning applications.

Experimental section

Materials

Ethylorthosilicate ($Si(OC_2H_5)_4$, TEOS, 98%), nonionic triblock copolymer pluronic P123 "Poly(ethylene oxide)-poly(propylene oxide)-poly(ethylene oxide)" $PEO_{20}PPO_{70}PEO_{20}$ average molecular weight (~5800), hydrochloric acid (HCl, 37%), cobalt(II) chloride hexahydrate ($CoCl_2$, $6H_2O$; 99%), ethanol (99.9%), tris(acetylacetonato)iron(III) ($Fe(acac)_3$; purity ≥98%), nickel(II) acetate tetrahydrate ($Ni(OCOCH_3)_2$, $4H_2O$; 98%), and tetracycline hydrochloride ($C_{22}H_{24}N_2O_8$, HCl; purity ≥95.0–102%), isopropanol (≥99.5%), *p*-benzoquinone (≥99%), and disodium ethylenediaminetetraacetate (EDTA-2Na, ≥99%), were all purchased from sigma-Aldrich and used as received.

Characterization

Fourier transform infrared (FTIR) spectra were obtained with a PerkinElmer Spectrum 100FT-IR spectrometer equipped with ATR accessory. The FTIR spectra were recorded in 4000–600 cm^{-1} with a resolution of 4 cm^{-1} and an accumulation of 32 scans. Solid-state cross-polarization magic angle spinning nuclear magnetic resonance of silicon and carbon spectroscopy (CP-MAS ^{29}Si NMR and CP-MAS ^{13}C NMR) were acquired on a JEOL JNM-ECZR 600 MHz spectrometer operating under cross-polarization conditions. UV spectra were recorded in the 200–800 nm range, with spectral on as the reference, using a PerkinElmer Lambda 1050 spectrometer equipped with an integrating sphere (Labshere, North Sutton, and USA). Textural properties were determined by N_2-physisorption analysis at 77 K on a Micromeritics Tristar III instrument. Before analysis, the samples were degassed under vacuum at 120 °C for 3 h. The specific surface area was determined using the multi point BET algorithm, the mesopore size distribution was determined by applying the BJH equation to the desorption branch, and the pore volume was determined at $p/p_0 = 0.95$, on the adsorption branch. The micropore surface and microporous volume were determined with the t-plot method. Thermogravimetric analysis (TGA) was performed on a discovery TGA analyzer using a heating rate of 10 °C min^{-1} from room temperature to 700 °C under air. Powder X-ray diffraction (XRD) was carried out by using a Bruker D8 Advance diffractometer with monochromatic Cu Kα source operated at 40 kV and 40 mA. Patterns were collected in steps of 0.02° (2θ) over the angular range 1–10.0°(2θ), with an acquisition time of 25 s per step. Scanning electron microscopy (SEM) coupled to energy dispersive X-ray (EDX) analyses were performed on a SEM-EDX instrument (FEI Quanta 250 FEG, Eindhoven, Netherlands). Transmission electron microscopy (TEM) images were acquired using a JEOL JEM 1400 electron microscope operating at 100 kV with a point resolution of 4.5 Å. XPS was measured on a SPECS spectrometer using a monochromatic X-ray source (Al and Mg) operating at 200 W. The metal loadings were determined by inductively coupled plasma optical emission spectroscopy (ICP-OES) using a Thermo Scientific instrument equipped with QTEGRA software. Prior to analysis, the solid samples were digested with a concentrated mixture of nitric acid/hydrochloric acid (3 : 1, v/v) at 120 °C for 4 h to ensure complete dissolution of the metal species. The resulting solutions were then diluted with ultrapure water. Quantification was carried out using external calibration with standard aqueous solutions. The emission lines monitored were 259.837 nm for Fe, 228.616 nm for Co, and 216.556 nm for Ni. Raman spectra were recorded using a confocal Raman spectrometer equipped with a 532 nm laser as the excitation source. The laser power at the sample surface was kept low (approximately 1–5 mW) to avoid local heating effects. Measurements were carried out at room temperature in the spectral range of 0–1200 cm^{-1}. The spectrum was obtained by averaging 3–5 accumulations, with an acquisition time of 10–30 s per accumulation. The samples were analysed in powder form without any additional pre-treatment. Temperature-programmed ammonia desorption (NH_3-TPD) experiments were performed on a Micromeritics Autochem II 2920 chemsorption analyzer instrument. The ammonia concentration in the output mixture was monitored using an OmnistarTM Pfeiffer mass spectrometer. Sample was pretreated at 300 °C under flowing argon (50 ml min^{-1}) for 1 h, and cooled to 100 °C then adsorbed to saturation by NH_3 for 0.5 h. Physically adsorbed ammonia was removed by flushing the sample with Ar (50 ml min^{-1}) for 2 h at 100 °C. Ammonia thermos-desorption was carried out in the temperature range 50–800 °C (10 °C min^{-1}). For the mineralization study, total organic carbon (TOC) degradation was measured using a TOC analyzer (Model:

TOC-LCPN, Shimadzu Co.). TOC (%) was calculated using the eqn (1):

$$\text{TOC}\ (\%) = \frac{\text{TOC}_0 - \text{TOC}_t}{\text{TOC}_0} \times 100 \quad (1)$$

where TOC_O (%) and TOC_t (%) represent the initial and time-t TOC concentrations, respectively. Photochemical stability and degradation tests were performed in a cylindrical, double-jacketed Pyrex reactor measuring 7 cm in diameter and 12 cm in height. It features two lateral openings for water circulation to maintain a homogeneous temperature. The irradiation source is a 230V 160W E27 PALLAS (Blended Mercury Lamp) positioned axially.

Synthesis of SBA-15_EXT and SBA-15

SBA-15 was prepared according to literature procedure.[20] In a typical procedure, pluronic 123 (P123) (4.0 g) was weighted into a 250 mL flask with stir bar. The polymer was dissolved by adding distilled water (30 mL), 2 M HCl (120 mL) and 4 h of vigorous stirring at 35 °C. Next TEOS (9.0 mL) was added dropwise *via* syringe. A fine white precipitate formed after 30 min, this solution was vigorously stirred at 35 °C for 24 h and then the suspension was heated for additional 48 h at 80 °C. The solution was filtered and the resulting "silica-pluronic" composite was dried first at room temperature (24 h) and then at 80 °C overnight. Template extraction was carried out *via* Soxhlet extraction using refluxing 95% EtOH (600 mL) for 5 days. The recovered silicate was dried at room temperature for 24 h and then at 80 °C for an additional 24 h. The harvested material will be denoted as **SBA_EXT**. Alternatively, pluronic-containing silica material was also thermally treated at 500 °C under air for 2 h, with a heating rate of 5 °C min^{-1}. The resulting material will be denoted as **SBA-15**.

Preparation of $^{x\%}$M@SBA-15

The catalysts were synthesized *via* the wet impregnation method. Appropriate amounts of nickel acetate, iron acetylacetonate, and cobalt chloride, corresponding to 5 wt% metal loading in the final material, were dissolved in 5 mL of ethanol. The soxhlet-treated **SBA-15_EXT** support was subsequently introduced into the solution, which was maintained at room temperature for 24 h and then at 40 °C for 48 h to ensure complete solvent evaporation. The resulting solid was finally calcined at 500 °C for 2 h with a heating rate of 5 °C min^{-1}.

Tetracycline removal

The adsorption capacity of the materials was assessed by monitoring tetracycline (TC) removal under dark conditions for 3 h. To prevent light-induced photo-degradation, all solutions were wrapped in aluminium foil. For kinetic studies, the initial TC concentration was set at 0.1 mmol L^{-1}, and 0.1 g of adsorbent was dispersed in 100 mL of the TC solution at room temperature. At predetermined time intervals, aliquots were collected, filtered through a 0.45 μm membrane, and the residual TC concentration was quantified using a pre-calibrated UV–vis spectrophotometer at the maximum absorption wavelength (λ_{max} = 360 nm). Each adsorption test was performed three time to check its reproducibility and the provided value averaged.

The concentration of tetracycline and its progressive adsorption were monitored using a UV–visible spectrophotometer at a wavelength of 360 nm. The adsorption capacity (mg g^{-1}), removal rate, and adsorption efficiency (Q_{ads}, %) were determined using eqn (2) and (3). In these equations, C_0 represents the initial concentration of the antibiotic solution (mg L^{-1}), C_t is the concentration at time t (mg L^{-1}), m is the adsorbent dosage (g), and V is the volume of the tetracycline wastewater, as defined below:

$$Q_t = \frac{C_0 - C_t}{m} \times V \quad (2)$$

$$Q_{ads}\ \% = \frac{C_0 - C_t}{C_0} \times 100 \quad (3)$$

The influence of pH on the adsorption process was evaluated by adjusting the solution to pH 3, 7, and 9 using hydrochloric acid (HCl) and sodium hydroxide (NaOH).

For the photo-degradation experiments, a tetracycline (TC) solution (1 mmol L^{-1}) was combined with 0.1 g of photo-catalyst and stirred magnetically in the dark for three hours to achieve adsorption equilibrium on the catalyst surface. The resulting suspension was subsequently irradiated for three hours. Post-irradiation, the samples were filtered through a Millipore membrane (0.45 μm), and the residual TC concentration was determined using a calibrated UV–visible spectrophotometer. Akin to the adsorption study, each photocatalytic test was triplicated and the result was assumed to be valuable only when yielding nearly the same performance ±5%; the provided value being averaged.

Recycling adsorption experiments were performed by recovering and thoroughly washed the spent adsorbent with distilled water (20 mL) and ethanol (20 mL) to remove pollutants. The material was then air-dried, followed by further drying in an oven at 80 °C for 2 h before reuse. For the photocatalysis experiments, the material was rather recovered and washed with sodium chloride solution (1 mol L^{-1}), air-dried at room temperature overnight, and subsequently subjected to thermal drying at 80 °C for one hour prior to reuse in the following cycle.

Results and discussion

1/Synthesis and characterization of metal oxide loaded mesoporous silica ($^{x\%}$M@SBA-15)

Pristine mesostructured **SBA-15** silica was prepared through hydrolysis and condensation of tetraethoxysilane around the self-assembled pluronic surfactant, followed by soxhlet extraction to remove the surfactant from the pores to lead to sample we will call **SBA-15_EXT**. Thermal treatment of the latter affords benchmarked **SBA-15**. Three metal oxide-containing high-surface area **SBA-15** were prepared by post-loading well-defined amount (x = 5wt.%) of the metal precursors [$CoCl_2$, ($Ni(OCOCH_3)_2$ and $Fe(acac)_3$] within **SBA-15_EXT**. Each material

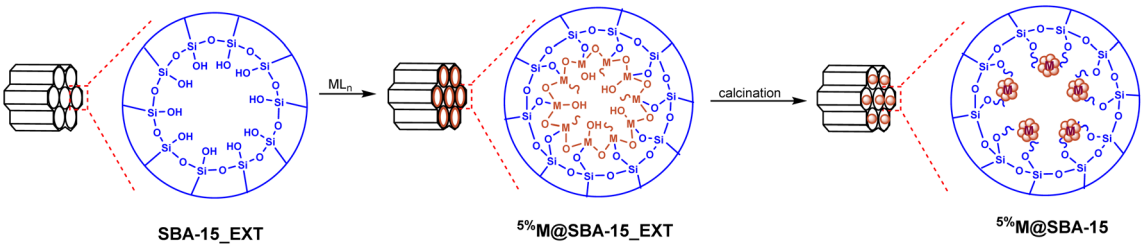

Fig. 1 Multistep preparation of $^{x\%}$M@SBA-15 (M = Co, Ni, and Fe).

was next isolated and oven-dried to yield **$^{x\%}$M@SBA-15_EXT** (M = Co, Fe, Ni). Next, they are subjected to thermal annealing at 500 °C under air for triggering the growth of nanosized metal oxide inside of the support, affording **$^{x\%}$M@SBA-15** (Fig. 1). As it will be commented below, additional loading of x = 2.5 wt.% and 7.5 wt.% were also prepared in the case of cobalt and further characterized. The resulting materials were subjected to a set of spectroscopic and textural analyses prior to their use as tetracycline removers from water.

DRIFT spectra of native **SBA-15** and metal oxide supported on **SBA-15** are represented in Fig. S1. Soxhlet extracted silica (**SBA-15_EXT**) displays an intense band centered at 1051 cm^{-1} and another one at 796 cm^{-1}, attributed to the asymmetric and symmetric stretching vibration mode of Si–O–Si. A narrow band characteristic of Si–OH groups was observed at 942 cm^{-1}, while the pattern of OH involved in hydrogen-bonding network appears as broad band at around 3357 cm^{-1}. The small band at 1629 cm^{-1} is assignable to physically adsorbed water, while the one at 2974 cm^{-1} could be attributed to C–H from residual pluronic or ethoxysilylated groups. Thermally treated **SBA-15** displays the same pattern with two noticeable differences, the first one being the significant reduction of the band at 942 cm^{-1} as a result of Si–OH dehydration through condensation to form stable Si–O–Si siloxane network, and the disappearance of the signal at 2974 cm^{-1} resulting from complete removal of the pluronic. In the metal loaded materials, the presence of the ligand around the metal was unambiguously characterized for **$^{5\%}$Fe@SBA-15_EXT** and **$^{5\%}$Ni@SBA-15_EXT** prior to their thermal treatment, with their signature being recognized in the DRIFT spectra (C–H and C=C at 2981 and 1523 cm^{-1}) and (C–H and C=O at 2979 and 1719 cm^{-1}) (Fig. S2). For thermally treated **$^{5\%}$Fe@SBA-15** and **$^{5\%}$Ni@SBA-15**, these signals disappear in favors of M–O–Si and M–O–M bonds formation. Besides, no change in the intensities of the bands at 3371 cm^{-1}, 1629 cm^{-1}, 1051 cm^{-1}, and 552 cm^{-1} could be observed after metal impregnation, compared to the pristine **SBA-15** support (Fig. S3).

^{29}Si MAS NMR and CP MAS spectra of the calcined silica (**SBA-15**) are presented in Fig. S4. ^{29}Si NMR spectra exhibit three typical signals of pure inorganic silicon holding the silica framework: the so-called Q^2 $(SiO)_2Si(OH)_2$, Q^3 $(SiO)_3Si(OH)$, and the fully condensed Q^4 sites $(SiO)_4Si$. ^{29}Si MAS NMR shows the presence of Q^4-type species centered at −109 ppm of Q^4 groups as dominating species in the bulk, while solid-state ^{29}Si CP MAS spectra evidence the presence of the Q^n-type silicon species on the surface, with Q^3 bearing one hydroxyl group being the most abundant.[21]

Solid-state ^{13}C NMR of Soxhlet-treated silica (**SBA-15_EXT**) (Fig. S5, and C1) shows signals corresponding to the pluronic structuring agent, with the one at 15.19 ppm being assigned to the methyl group of the hydrophobic block, a signal at 71.93 ppm is assigned to the –CH group, while the one at 74.81 ppm corresponds to the –CH_2 group of the same hydrophobic block. The signal resonating at 69.31 ppm is assigned to the –CH_2 group of the hydrophilic block. This indicates that the pluronic was not completely removed by soxhlet extraction as already observed by DRIFT analysis. Total removal of the pluronic surfactant through soxhlet extraction has been previously reported to be impossible, a fact attributed to the occlusion of the latter in poorly accessible and weakly exposed areas (*ex.* micropores).[22,23] In addition to the pluronic signals, two additional signals appear at 15 ppm and 57.25 ppm, corresponding to Si(OEt) formed probably through ethanolysis of the exposed surface silanols (Si–OH) during soxhlet extraction. In turn, no pluronic-related signals could be observed in the calcined silica (**SBA-15**), confirming its complete elimination by thermal oxidative treatment (Fig. S5, C2). Thermogravimetric analysis (TGA) of **$^{5\%}$M@SBA-15_EXT** display typical weight degradation pattern of organic–inorganic materials in agreement with the persistence of organic ligands in the mesostructure. The share residue at 700 °C varies between 64% and 72% (Fig. S6 and Table S1). The lowest weight loss was observed for **$^{5\%}$Co@SBA-15_EXT** and is attributed to the inorganic nature of residual chloride instead of the acetylacetonate remaining in the case of iron or acetate used in the case of nickel that induce further weight degradation. The weight loss observed for **$^{5\%}$Co@SBA-15_EXT** corresponds merely to the removal of volatiles below 100 °C (physisorbed water) and surface ethoxy groups (between 100 and 200 °C). TGA of the calcined materials (**$^{5\%}$M@SBA-15**) shows comparatively an increase in the share residue at 700 °C for the three materials up to 84% and 88%, in consistency with their inorganic nature (Fig. S6 and Table S1). While metal impregnation occurs through interaction with surface silanols leading to their consumption, such modification did not compromise the surface polarity/wettability of the resulting materials, as no change in their dispersion has been noticed (see digital photos in Fig. S7). A plausible explanation could be the possible presence of hydroxyl defects from both Si–OH and M–OH on the surface of the final particles.

The amount of loaded metal was estimated using ICP analysis, showing a metal content of 5.19 wt%, 4.54 wt% and 4 wt%

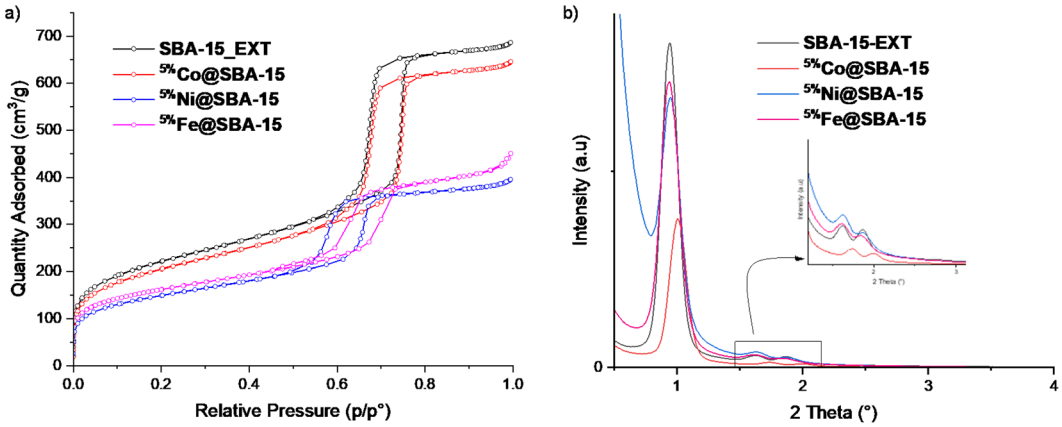

Fig. 2 N_2 adsorption–desorption isotherms (a) and low angle XRD (b) of metal-loaded $^{5\%}$Co@SBA-15, $^{5\%}$Ni@SBA-15 and $^{5\%}$Fe@SBA-15 *versus* pristine SBA-15_EXT.

for Co, Ni and Fe, respectively. These values are nearly comparable to the starting composition.

Nitrogen adsorption–desorption isotherms of **$^{5\%}$M@SBA-15** are plotted against the one of the pristine supports (Fig. 2a). Regardless of the metal precursor, the three materials display type-IV isotherms with strong capillary condensation at high relative pressure and H_1 hysteresis loops, typical of 2D hexagonal symmetry of mesoporous materials,[24,25] with large pore diameters and narrow size ranges. An increase in the specific surface area of the pristine mesostructure along with a significant pore diameter expansion were noticed when comparing soxhlet-extracted **SBA-15_EXT** solid ($S_{BET} = 774$ m^2 g^{-1}; $D = 6.15$ nm) *versus* thermally-annealed **SBA-15** material ($S_{BET} = 844$ m^2 g^{-1}; $D = 6.6$ nm) (Table 1). While thermal treatment normally triggers silanol condensation to form condensed siloxane network, and consequently, significant wall and framework shrinkage and compactness that could reduce the specific surface area, this phenomenon was counterbalanced by the significant removal of residual pluronic during thermal treatment, bringing additional empty space for porosity enhancement. As mentioned above, soxhlet extraction never removes completely the pluronic from the pores. However, we intentionally did not force further its removal as residual pluronic should interact with metal precursors, providing additional means for forming ultra-small and discrete metal nanoparticles.[26] In the loaded materials, a significant decrease of the specific surface area was noticed upon metal loading: $S_{BET} = 722$ m^2 g^{-1} for **$^{5\%}$Co@SBA-15**, $S_{BET} = 524$ m^2 g^{-1} for **$^{5\%}$Ni@SBA-15** and $S_{BET} = 576$ m^2 g^{-1} for **$^{5\%}$Fe@SBA-15** (Table 1). The absence of severe reduction in the pore diameter with respect to the pristine **SBA-15** support suggests a uniform distribution of the entrapped metal oxide in the surface, with more species being bonded to surface silanols to form Si–O–M bridges. This bonding situation is expected to minimize the formation of monophasic metal oxide that could grow during thermal treatment in the empty space direction and could clog the pores. The marginal variation of the textural properties of **$^{5\%}$Co@SBA-15** in spite of its high metal loading (based on ICP measurement) suggests that the latter display the smallest size of metal nanoparticles and/or a better dispersion within the support, compared to its analogues loaded on **$^{5\%}$Ni@SBA-15** and **$^{5\%}$Fe@SBA-15**.

To further elucidate the pivotal role of residual pluronic and surface silanol groups in stabilizing cobalt clusters and preserving the mesostructured framework, the same incipient wetness cobalt impregnation was carried out on fully calcined **SBA-15**, which is devoid of pluronic residues and bears a comparatively lower density of surface silanols. Following metal loading, the resulting material was subjected to an identical thermal treatment. Strikingly, a dramatic decrease in the specific surface area was observed, dropping to 6 m^2 g^{-1}. This collapse is attributed to the uncontrolled thermal growth

Table 1 Textural characteristics of SBA-15_EXT, SBA-15 and $^{x\%}$M@SBA-15

	XRD		Nitrogen sorption				
Samples	d_{100} (Å)	a (Å)	S_{BET} (m^2 g^{-1})	V_{mesop} (ml g^{-1})	Pore diameter (Å)	Wall thickness (Å)	Metal loading %
SBA-15_EXT	94	108.5	774	0.97	61.5	47	—
SBA-15	98	113	844	1.08	66	47	—
$^{5\%}$Co@SBA-15	88	101.8	722	0.93	69	32.8	5.19
$^{5\%}$Ni@SBA-15	93	107.4	524	0.62	49	58.4	4.54
$^{5\%}$Fe@SBA-15	95	109.6	576	0.62	53.7	55.9	4

of cobalt species, which expand within and ultimately obstruct the otherwise empty porous network (Fig. S8).

The retention of ordered mesostructured was further corroborated using low-angle X-ray diffraction (XRD), with the patterns of the parent **SBA-15**, and the corresponding metal loaded **$^{5\%}$Co@SBA-15**, **$^{5\%}$Ni@SBA-15** and **$^{5\%}$Fe@SBA-15** being presented in Fig. 2b. All of them show three diffraction peaks of [100], [110], and [200] plan, respectively located at $2\theta = 0.94°$, 1.62°, 1.86°. These peaks are typical of mesoporous structure displaying 2-D hexagonal (P_6mm) symmetry. Their persistence after metal impregnation confirms the retention of the mesostructure after loading and reflects the stability of the decorated mesopores during thermal annealing treatment.[27] However, metal impregnation with Ni, Fe, Co decreases the intensity of the peak at 0.94° indicating a slight ordering decrease upon metal (oxide) loading. A significant shift of that peak (from 0.94° to 1°) was also observed exclusively for **$^{5\%}$Co@SBA-15** that could reflect a slight shrinkage of the lattice, probably due to the effect of metal particle size in the X-ray scattering.[28]

We further investigated the morphology of the resulting materials using SEM coupled to EDX mapping as well as TEM analyses (Fig. 3). Irrespective to the nature of the grown metal oxide inside of the mesostructure, SEM analyses show a typical rod-like morphology of **SBA-15** for all these materials, clearly indicating the retention of the mesostructured network during metal impregnation and thermal annealing treatment (Fig. 3a).[29–32] However, slight shape alteration was observed for **$^{5\%}$Ni@SBA-15** where aggregated spherical particles seem to disturb the rods continuity. In line with these observations, we noticed that **$^{5\%}$Ni@SBA-15** displays the lowest specific surface area and the lowest pore diameter. EDX mapping unambiguously confirm the presence of the metal (oxide) on the mesostructure, with a nice pattern of distribution, excluding aggregation or preferential location within the silica framework (Fig. 3b).

The resulting materials were next investigated by TEM to gain a better understanding on the structure at the nanoscale. Fig. 3c shows TEM images for **$^{5\%}$Ni@SBA-15**, **$^{5\%}$Co@SBA-15** and **$^{5\%}$Fe@SBA-15**, with the corresponding particle size histograms being presented in the onset of each photo. Akin to pristine **SBA-15**, TEM images of the metal-loaded **SBA-15** reveal a highly ordered hexagonal mesoporous structure, indicating that the periodic order remains intact after metal impregnation and thermal treatment. These findings are consistent with nitrogen adsorption analysis, which confirms the presence of a hexagonal mesoporous arrangement. Moreover, the discrete darker contrast areas observed within the channels most likely correspond to Co, Ni, and Fe nanoparticles smaller than 1 nm, exhibiting a highly homogeneous dispersion, as shown in Fig. 3c. The size of the particles was found to be 0.47 ± 0.15 nm for **$^{5\%}$Ni@SBA-15**, 0.63 ± 0.17 nm for **$^{5\%}$Co@SBA-15** and 0.73 ± 0.18 nm for **$^{5\%}$Fe@SBA-15**. The great dispersion of the dark spots is evident in the case of **$^{5\%}$Co@SBA-15** along the channels, which perfectly agree with its high surface area and opening porosity, comparable to the one of the pristine support, in spite of the highest cobalt loading reached with respect to nickel and iron.

We next attempted to unveil the nature of the metal phase grafted on the silica mesostructure using wide-angle XRD and complemented by RAMAN and X-ray photo-electronic

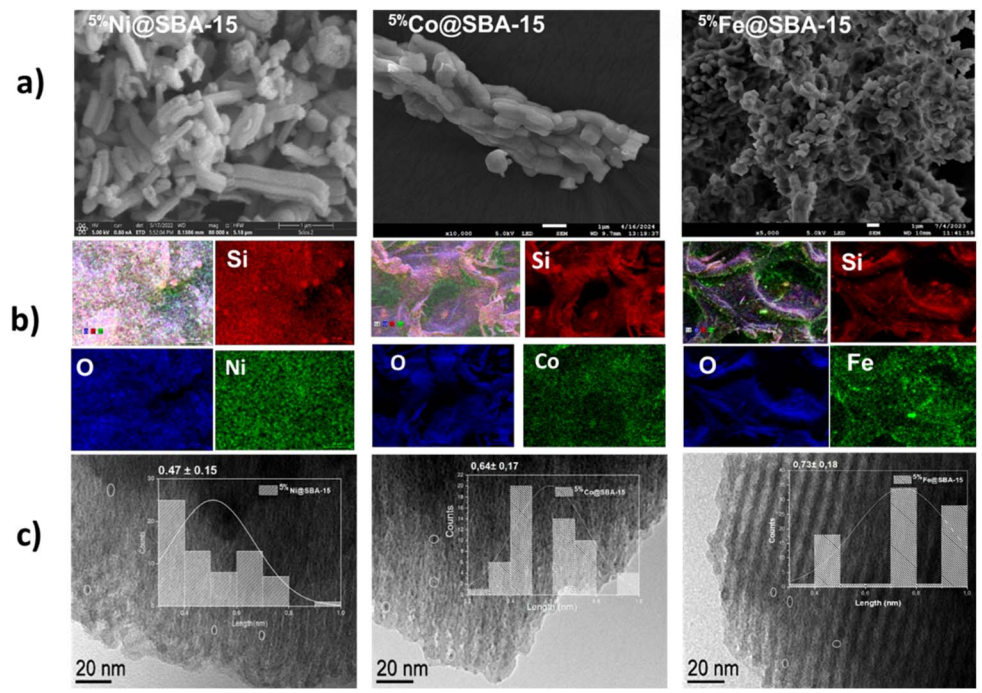

Fig. 3 Scanning and transmission electronic microscopy of **$^{5\%}$Ni@SBA-15**, **$^{5\%}$Co@SBA-15** and **$^{5\%}$Fe@SBA-15**. (a) SEM, (b) EDX mapping of oxygen, silicon and the metal for each material, and (c) TEM images and histograms of the size distribution of the corresponding metal nanoparticles.

spectroscopies in the special case of cobalt loaded silicates. Wide-angle XRD analysis was undertaken from 2θ value of 10° to 80° (Fig. S9). The broad diffraction peak between 15° and 30° is attributed to the amorphous silica network of the silica support.[33] For **$^{5\%}$Co@SBA-15**, the diffraction peaks at 2θ = 36.85° and 39.29° are assigned to cubic spinal phase of Co_3O_4 formed after calcination.[34] In the case of **$^{5\%}$Fe@SBA-15** and **$^{5\%}$Ni@SBA-15**, no peaks could be detected on the wide-angle spectra, meaning that the resulting metal oxide exists in its amorphous state, and/or that the crystallite size is below the detection limit. A reasonable explanation could be rooted on the formation of abundant Si–O–M seeds inside of the confined mesopores during the early stage of the impregnation, thereby restricting the thermodynamically favorable expansion of the metal (oxide) expected during thermal treatment.[35]

X-ray photo-electronic spectroscopy (XPS) was used to get additional insight on the chemical composition and surface chemistry of **$^{5\%}$Co@SBA-15**, considering its outstanding performance compared to its congeners as it will be commented below. The spectrum survey shows the presence of carbon, oxygen, silicon and cobalt elements on the surface of **$^{5\%}$Co@SBA-15**, corresponding to their binding energy labels (Fig. S10). Si 2p peaks patterns were fitted with 2 peaks ascribable to Si–O–Si and Si–O–H in descending by area of the peaks. O(1s) binding energy can be divided into three peaks at 531.4 eV, 533.2 eV, and 533.8 eV, corresponding to lattice oxygen (O_{latt}), surface adsorbed oxygen species (O_{surf}), and adsorbed molecular H_2O.[36] Fig. 4 shows the narrow scan spectrum for Co 2p peaks, with two major binding energy features around 781.9 and 798 eV attributed to Co $2p_{3/2}$ and Co $2p_{1/2}$, respectively. In addition, the Co $2p_{3/2}$ satellite peak at 786.6 ev proves the presence of Co^{2+}. The Co $2p_{3/2}$ peak can be decomposed into two peaks at 781.5 ± 0.2 eV and 782.8 ± 0.2 eV, which can be attributed to Co^{2+} and Co^{3+}.[37,38]

RAMAN spectroscopy provides additional information by showing typical signature of both siloxane framework and cobalt species (Fig. S11). Plotting the spectra of bulk Co_3O_4 against **$^{5\%}$Co@SBA-15** suggests the presence cobalt predominantly as a mixed Co^{2+}/Co^{3+} oxide. The signal at nearly 691 cm^{-1} suggests the presence of an ultra-small crystalline spinel structure, where the Co^{2+} cations occupy the tetrahedral site and the Co^{3+} species are located on the octahedral site.[39] However, this signature could also reflect the presence of distorted Co–O–Si modes, with such typical resonance being mainly observed when cobalt was atomically dispersed in high surface area carrier. Notably, the broadening and reduced intensity of the bands assigned to **$^{5\%}$Co@SBA-15** compared to bulk Co_3O_4 indicate the ultra-small size and/or high dispersion of the cobalt within the SBA-15 mesoporous matrix.[40]

Insight on the surface reactivity of these materials was gained using temperature programmed ammonia desorption (NH_3-TPD) (Fig. 5). Consistent with its lower surface reactivity,[41] thermally treated **SBA-15** shows a negligible amount of desorbed ammonia (0.0264 mmol g^{-1}). In turn, metal loaded samples exhibit a significant desorption peak in the range of 200–300 °C, indicating the presence of weak to moderate acid sites. None of the samples show however a distinct peak above 500 °C, assignable to strong acid sites. Therefore, the acidity of the samples is primarily low to moderate, which is characteristic of metal oxide impregnated mesoporous materials.[42,43] **$^{5\%}$Co@SBA-15** shows the largest amount of desorbed ammonia (0.6293 mmol g^{-1}) with the desorption peak being the highest in intensity among the series, indicating the presence of a greater number of acid sites compared with the other samples. **$^{5\%}$Ni@SBA-15** and **$^{5\%}$Fe@SBA-15** display similar quantities of desorbed ammonia (0.4851 and 0.4792 mmol g^{-1}, respectively). It is indeed obvious that the metal oxide loading imparts the resulting materials with improved Lewis acidity, with those generated in **$^{5\%}$Co@SBA-15** being apparently the most reactive.

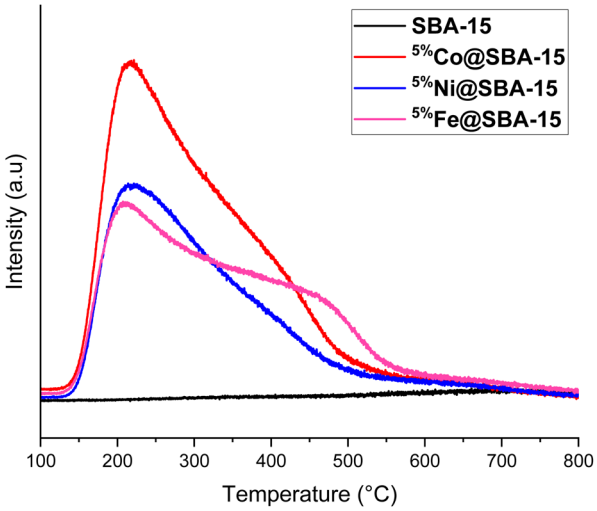

Fig. 5 NH_3-TPD profile of **$^{5\%}$Ni@SBA-15**, **$^{5\%}$Co@SBA-15** and **$^{5\%}$Fe@SBA-15** plotted against the one of the pristine SBA-15 support.

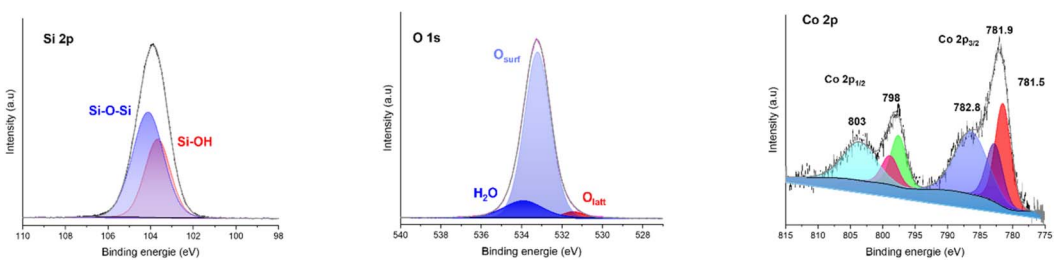

Fig. 4 XPS spectra of the Si 2p, O 1s, and Co 2p peaks of **$^{5\%}$Co@SBA-15**.

UV-visible spectroscopy reveals a different pattern of $^{5\%}$**M@SBA-15** when plotted against the one of the pristine **SBA-15_EXT** support, in consistency with the presence of visible light activatable metal oxide (Fig. S12). $^{5\%}$**Co@SBA-15** sample exhibits a shoulder extending from 200 nm into the visible region, whereas distinct absorption maxima are observed for $^{5\%}$**Ni@SBA-15** at 301 nm and for $^{5\%}$**Fe@SBA-15** at 217 nm and 260 nm (Fig. S12). Assuming a direct allowed transition, the Tauc plot calculated for $^{5\%}$**Co@SBA-15** yields an apparent optical band gap of ~4.32 eV (Fig. S13). This large optical band gap value is inconsistent with metallic Co^0, which lacks a band gap, and with CoO or Co_3O_4, which exhibit absorption onsets below 3 eV. Instead, this high band-gap value is characteristic of highly dispersed cobalt species interacting with the silica framework, where the optical response is dominated by ligand-to-metal charge-transfer transition, possibly through Co–O–Si interfacial states, isolated cobalt ions or ultra-small clusters at the frontier with well-isolated single atom species.[44,45]

Besides 5 wt% loading, two other materials with 2.5 wt% and 7.5 wt% were prepared. Nitrogen sorption analysis shows surface areas of 753 m^2 g^{-1} and 654 m^2 g^{-1}, pore diameter of 6.2 nm and 6.1 nm and pore volume of 0.95 cm^3 g^{-1} and 0.87 cm^3 g^{-1}, for $^{2.5\%}$**M@SBA-15** and $^{7.5\%}$**M@SBA-15**, respectively (Fig. S14 and Table S2). The specific surface area seems to slightly decrease with increasing metal loading from 2.5 wt.% to 5 wt.% to 7.5 wt.%. In spite of that, no significant alteration of the mesostructure ordering could be observed, indicating that the primary difference lies in the amount of the metal oxide exposed on the surface.

2/Tetracycline removal over metal oxide loaded mesoporous silica ($^{x\%}$M@SBA-15)

With these materials in hand, we embarked to assess their reactivity towards tetracycline uptake from water solution. Metal oxide supported on mesoporous silicates ($^{5\%}$**M@SBA-15**) were compared with soxhlet-extracted **SBA-15_EXT** and thermally-annealed **SBA-15** and the results are shown in Fig. 6a.

Monitoring tetracycline uptake revealed that the plateau was reached after 180 minutes, which was then established as the duration for subsequent experiments. **SBA-15_EXT** exhibits an uptake of 18%, while **SBA-15** shows an uptake of 16%. This minor variation ruled out the subtle difference on the inherent texture and surface properties of the two supports in terms of Si–OH density. In sharp contrast, metal oxide-loaded materials show significantly better performance, with both iron, nickel and cobalt-loaded **SBA-15** recording an impressive 85–86% tetracycline uptake. The presence of metal oxide increases the number of adsorbing sites compared to the Si–OH groups available on **SBA-15_EXT** and **SBA-15**. The amplified adsorption can likely be attributed to the Lewis acidity imparted by metal oxide loading, as substantiated by TPD measurements, which promotes strong interactions with the donor and basic sites present in tetracycline. Despite their effectiveness, $^{5\%}$**Fe@SBA-15** displayed some instability issues at long term exposure, where fluctuation in pollutant uptake could be seen after 3 hours, while $^{5\%}$**Ni@SBA-15** faced inconsistencies during

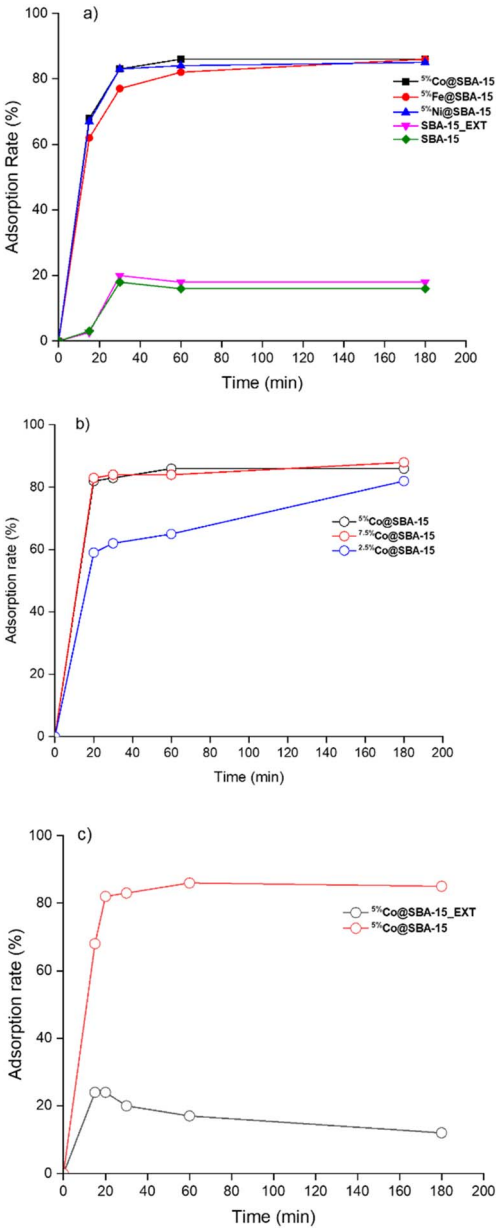

Fig. 6 Adsorption kinetics for tetracycline removal (C = 10^{-4} mol l^{-1}) from water. (a) Adsorption of $^{5\%}$Co@SBA-15, $^{5\%}$Fe@SBA-15 and $^{5\%}$Ni@SBA-15, soxhlet-extracted SBA-15_EXT and thermally-annealed SBA-15. (b) The effect of metal loading on tetracycline uptake over $^{2.5\%}$Co@SBA-15, $^{5\%}$Co@SBA-15 and $^{7.5\%}$Co@SBA-15. (c) Adsorption kinetics of $^{5\%}$Co@SBA-15_EXT *versus* $^{5\%}$Co@SBA-15.

reproducibility experiments. In contrast, $^{5\%}$**Co@SBA-15** demonstrated consistent performance, maintaining reproducible results without significant deviations that could undermine reliability. Several factors acting alone or in combination could explain this tendency, including possible weak interfacial interplay of iron oxide and nickel oxide with the pristine silica support, as well as the leaching of the active phase to the solution. We have consequently decided to exclusively continue with cobalt oxide loaded on mesoporous silica.

We next investigate the effect of metal loading on tetracycline removal efficiency using $^{2.5\%}$**Co@SBA-15**, $^{5\%}$**Co@SBA-15**

and **$^{7.5\%}$Co@SBA-15**. The three materials achieve 82 to 88% tetracycline removal after 3 hours (Fig. 6b). However, **$^{2.5\%}$Co@SBA-15** displays the lowest adsorption kinetics, compared to its congeners. When comparing **$^{5\%}$Co@SBA-15** and **$^{7.5\%}$Co@SBA-15**, the nearly similar adsorption kinetics could reflect an optimal coverage of the silica surface at 5 wt.%, and that no additional adsorbing sites could be further generated above such loading. Beyond 5 wt.%, the additional amount of cobalt could grow on the top of the first monolayer, as reflected by the slight reduction of the pore diameter from 6.9 nm for **$^{5\%}$Co@SBA-15** to 6.1 nm for **$^{7.5\%}$Co@SBA-15**. Chemically speaking, at an optimal coverage, all silanols are assumed to be consumed to form Si–O–Co, while adding more cobalt precursor affords additional Co–O–Co. Reasonably, one might invoke the importance of Si–O–Co bridges as reactive sites considering that from active metal basis, no additional reactivity emanates from Co–O–Co.

We have also tested the performance of cobalt loaded **SBA-15** prior to its calcination. After three hours, the untreated material (denoted as **$^{5\%}$Co@SBA-15_EXT**) adsorbed only 12% of the tetracycline, compared to 86% uptake recorded for the calcined **$^{5\%}$Co@SBA-15** material (Fig. 6c). Prior thermal annealing, the impregnated metal is supposed to be on its molecular state, being weakly ligated to the surface through hydrogen bonding, with the formation of minor bridges through Si–O–Co. Besides, cobalt is also supposed to be linked to chloride. This vulnerable bonding situation could explain the decrease in the tetracycline uptake from the maximum of 22% after 20 minutes, most probably because of the leaching of weakly bonded cobalt species from the silica surface to the liquid solution. The final uptake stabilizes at nearly 12%, coinciding with the uptake recorded by pristine **SBA-15** support, which further consolidate our assumption on cobalt leaching to restore the pristine support. Thermal annealing treatment allows indeed for simultaneous embedding of cobalt on the walls to create more abundant and stronger Si–O–Co bridges, while triggering the growth of cobalt nanoparticles by bringing the metal one to each other. ICP analyses further corroborate these assumptions by ruling out the occurrence of cobalt leaching after adsorption experiments, thus providing salient evidence for the strong embedding of the metal clusters inside of the mesostructured silica network. Being located inside of the pores of the support, such confined environment restricts the growth of the metal oxide and keeps its size at the nanoscale, resulting in high Lewis-acid materials that promote better tetracycline adsorption. The merits of these materials could be indeed summarized in combining high-surface area from **SBA-15** and Lewis acidity from discrete cobalt oxide grown on the surface. In support to this holistic performance, the use of pure Co_3O_4 solid material failed to record acceptable tetracycline uptake (<4%), ruling out any inherent adsorptive cobalt properties (Fig. 7).

To unveil the role of surface polarity that could involve additional hydrogen bonding, we have subjected **$^{5\%}$Co@SBA-15** to reaction with hexamethyldisilazane. This reagent is known to convert residual surface silanols (Si–OH) into Si–O–$SiMe_3$, thereby switching the well-established polar silica surface to hydrophobic support. DRIFT analysis confirmed the

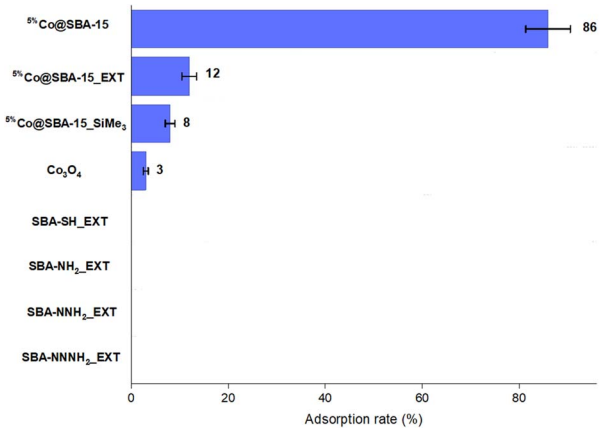

Fig. 7 Adsorption of tetracycline after $t = 180$ min using various SBA-15-type materials (SBA-NH_2_EXT, SBA-NNH_2_EXT, SBA-$NNNH_2$_EXT, SBA-SH_EXT), Co_3O_4, $^{5\%}$Co@SBA-15_EXT, $^{5\%}$Co@SBA-15 and $^{5\%}$Co@SBA-15_$SiMe_3$.

appearance of new peaks at 2963 and 2847 cm^{-1} (corresponding to the C–H stretching vibrations of methyl groups), at 1405 cm^{-1} (methyl C–H bending vibration), and at 843 cm^{-1} (Si–C stretching vibrations). In addition, a significant decrease in the intensity of the peak around 3367 cm^{-1}, attributed to Si–OH stretching, after passivation further indicates that successful silylation occurred on the surface of the support (Fig. S15). Solid-state ^{13}C NMR spectra show a distinct peak around 0 ppm very characteristic of trimethylsilyl groups,[46,47] which confirm that hexamethyldisilazane has effectively reacted with surface silanol groups (Si–OH) (Fig. S16). The resulting material denoted as **$^{5\%}$Co@SBA-15_$SiMe_3$** was next used to adsorb tetracycline. Contrasting with its pristine **$^{5\%}$Co@SBA-15** material, the hydrophobically designed trimethysilylated **$^{5\%}$Co@SBA-15_$SiMe_3$** removes only 8% tetracycline from water after exposure for three hours (Fig. 7). This points to the role of surface polarity in attracting tetracycline near to the adsorbing sites, while the bulky trimethylsilyl seems to sterically hinder tetracycline for approaching the silica surface.

For comparison, we have also prepared four organofunctionalized silica supports, namely, aminopropyl-modified **SBA-15** (denoted as **SBA-NH_2_EXT**), *N*-(propyl) ethylenediamine-modified **SBA-15** (denoted as **SBA-NNH_2_EXT**), *N*-(propyl)diethylenetriamine-modified **SBA-15** (denoted as **SBA-$NNNH_2$_EXT**), and mercaptopropyl-modified **SBA-15** (**SBA-SH_EXT**) (see Fig. S17, 18, 19 and Table S3 for their characterization). These materials were next used as adsorbents of tetracycline from aqueous solution. Surprisingly, none of them yielded interesting results, with the maximum tetracycline uptake did not exceed more than 3%. These findings definitely highlight the superiority of cobalt (oxide) loaded **SBA-15** for quantitative removal of pharmaceutical tetracycline from water compared to pristine **SBA-15**, organomodified **SBA-15**, trimethylsilylated **$^{5\%}$Co@SBA-15_$SiMe_3$**, as well as pure Co_3O_4 metal oxide (Fig. 7).

Adsorption kinetics were next evaluated by fitting experimental results with pseudo-first order and pseudo-second order

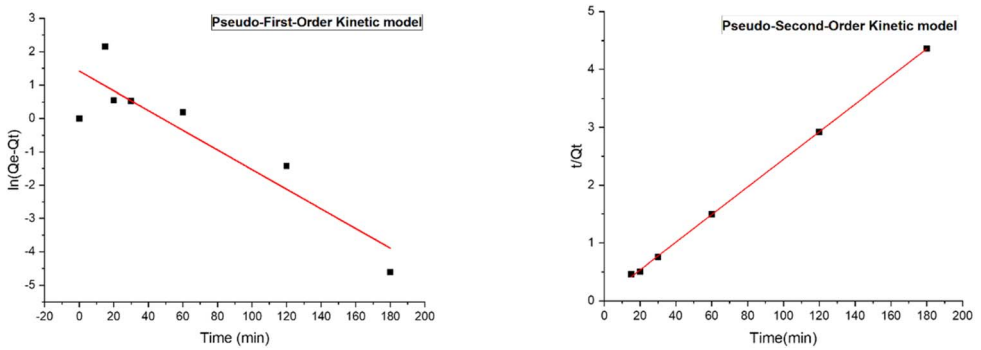

Fig. 8 Pseudo-first-order and pseudo-second order model of tetracycline adsorption over $^{5\%}$Co@SBA-15 material.

model. Pseudo-first order (PFO) (eqn (4)) is applied to estimate the adsorption at the early stage of the phenomena while pseudo-second order (PSO) theory (eqn (5)) predicts that chemisorption is a rate-limiting process. The nonlinear equations of the two mentioned models are presented below, were Q_e (mg g^{-1}) and Q_t (mg g^{-1}) refer to adsorption capacities at equilibrium and time t, respectively. K_1 (l/min) and K_2 are the rate constant of PFO and PSO, respectively.

$$\ln(Q_e - Q_t) = \ln Q_e - K_1 t \quad (4)$$

$$\frac{t}{Q_t} = \frac{1}{K_2 Q_e^2} + \frac{t}{Q_e} \quad (5)$$

The results are illustrated in Fig. 8 and the obtained fitting parameters are provided in Table 2. The extracted data properly fit with the pseudo-second-order kinetic, compared to first-order kinetics, as illustrated by its higher correlation coefficient ($R^2 = 0.99$) nearly close to 1. Also, Q_e value deduced from the PSO model (41.8 mg g^{-1}) was close to the experimental ones (41.31 mg g^{-1}), in opposite to the value derived from PFO model (4.12 mg g^{-1}), indicating that the adsorption process fits the pseudo-second-order model well.[48] This means that chemisorption is the dominant factor in the adsorption process, much probably through chemical interaction of tetracycline functionalities with both Lewis and Brønsted acid sites located on the material surface.

The experimental results were next simulated using the Langmuir model (eqn (5)), and the Freundlich model (eqn (6)). In the formula, Q_e (mg g^{-1}) and Q_m (mg g^{-1}) are the adsorption capacities at the equilibrium and the maximum capacity of the adsorbent, respectively. C_e is the equilibrium concentration of the antibiotic (mg L^{-1}). K_L (L mg^{-1}), and K_F are the Langmuir adsorption constant and Freundlich adsorption constant. These parameters correspond to the maximum binding energy (J mol^{-1}).[49,50]

Table 2 First-order and second-order kinetic fitting

Kinetic model	Q_e^{exp}	Q_e^{cal}	K	R^2
PFO	41.31	4.12840032	−0.0001639	0.91056
PSO	41.31	41.8760469	0.00974627	0.99975

$$\frac{C_e}{Q_e} = \frac{C_e}{Q_m} + \frac{1}{Q_m K_L} \quad (6)$$

$$\ln Q_e = \ln K_F + \frac{1}{n} \ln C_e \quad (7)$$

Equilibrium adsorption data for tetracycline over $^{5\%}$**Co@SBA-15** and the results of linear fitting of the Langmuir and Freundlich models are shown in Fig. 9 and Table 3.

Langmuir's model suggests that the adsorption process occurs as monolayer coverage on a homogeneous surface while the Freundlich model assumes the involvement of heterogeneous systems possessing non uniform sites with different binding energies. As shown in Table 3, the experimental data better fits with Freundlich model, as illustrated by its R^2 of 0.98 being closer to 1 compared to R^2 of 0.92 deduced from the Langmuir model. A plausible explanation could be the existence of two different acidic sites: (i) moderate to strong Lewis acidity from cobalt oxide clusters, being prone to accept an electron in their empty d orbital, and (ii) weak Brønsted acid sites remaining on the surface of silanols (Si–OH) and metalols (M–OH), known also to trigger hydrogen bonding. The constant K_F derived from the Freundlich isotherm represents the adsorption capacity, and the value of n represents the favorability of the adsorption process.[51] In support to these assumptions, tetracycline uptake has been hindered upon surface passivation with trimethylsilyl groups ($^{5\%}$**Co@SBA-15_SiMe$_3$**) as previously discussed. Under such circumstances, the donation of nitrogen belonging to tetracycline towards Lewis acidic cobalt oxide nanoclusters and the interaction of the pharmaceutical with the surface through hydrogen bonding become with high thermodynamic penalty as most of the involved sites were consumed and replaced by bulky and somewhat inert trimethysilyl groups that induce significant steric hindrance against any chemical guest.

We have also investigated tetracycline uptake over $^{7.5\%}$**Co@SBA-15** at two additional pH levels of pH = 3 and pH = 9, and compared the obtained results with those reached under neutral pH conditions (Fig. 10). Notably, tetracycline is typically an amphoteric antibiotic, with its molecular structure being sensitive to pH variation, affecting both the existing forms of TC and the generation of the oxidative species. Interestingly,

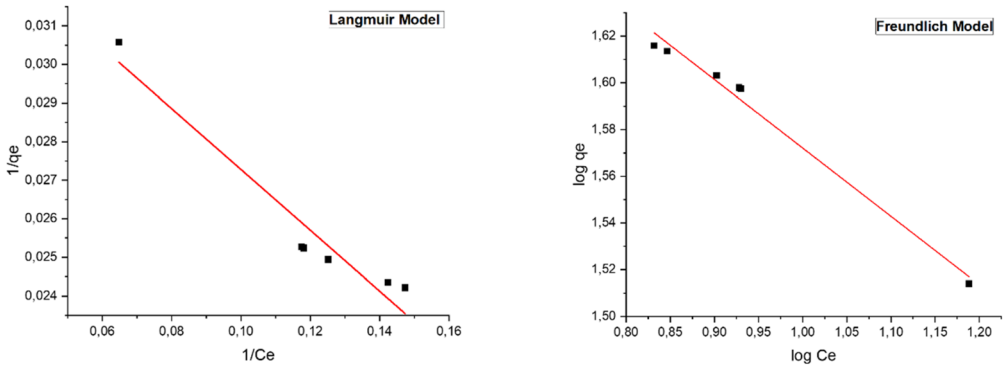

Fig. 9 Langmuir and Freundlich models.

Table 3 Comparative study of Langmuir and Freundlich adsorption isotherms

Langmuir			Freundlich		
Q_{max}	K_L	R_2	K_F	$1/n$	R_2
28.4333239	−0.4456976	0.92226	73.2925784	−3.4136683	0.98247

$^{7.5\%}$Co@SBA-15 operates with efficiency over a wide range of pH values. At neutral and basic pH, the adsorbent removes nearly 88% and 86% respectively. At pH = 3 where protonation of tetracycline is expected to occur, the recorded uptake was of 80%.

Zeta potential of **$^{7.5\%}$Co@SBA-15** reaches its maximum at pH = 2, and then progressively decreases with increasing pH values to reach neutrality at pH (7.5–7.7) (pHpzc) (Fig. S20). When the pH of the solution is indeed higher than pHpzc, the adsorbent's surface is negatively charged, and conversely, if pH is lower than pHpzc, the surface of the adsorbent is positively charged. At pH = 3, the adsorbent surface is positively charged according to PZC analysis, and the tetracycline is positively charged too, with its main form being TCH^{3+}. Electrostatic repulsion between the positively charged surface and the cationic tetracycline occurs, which could explain the reduced uptake compared to neutral and basic pH. However, adsorption still significant suggesting its occurrence through other complementary mechanisms (*ex.* acid-base interaction). At neutral pH, the surface is close to neutrality, so electrostatic forces are weakened. Tetracycline, in its zwitterionic form, can interact through hydrogen bonds and van der Waals forces with the adsorbent surface, affording a great adsorption uptake (88%). At pH 9, the surface is negatively charged, attracting tetracycline in its anionic TC^{2-} (negatively charged) form. While repulsion with anionic tetracycline is envisioned, the abundance of polar and hydrogen donating sites from both the adsorbent and the pharmaceutical enables effective reduction (86%). This clearly consolidates the fact that besides anion exchange, tetracycline interacts with the adsorbent surface through different modes, including hydrogen bonding, and acid-base interaction.

FTIR spectra of **$^{5\%}$Co@SBA-15** was plotted against the one isolated after tetracycline adsorption (Fig. S21). The appearance

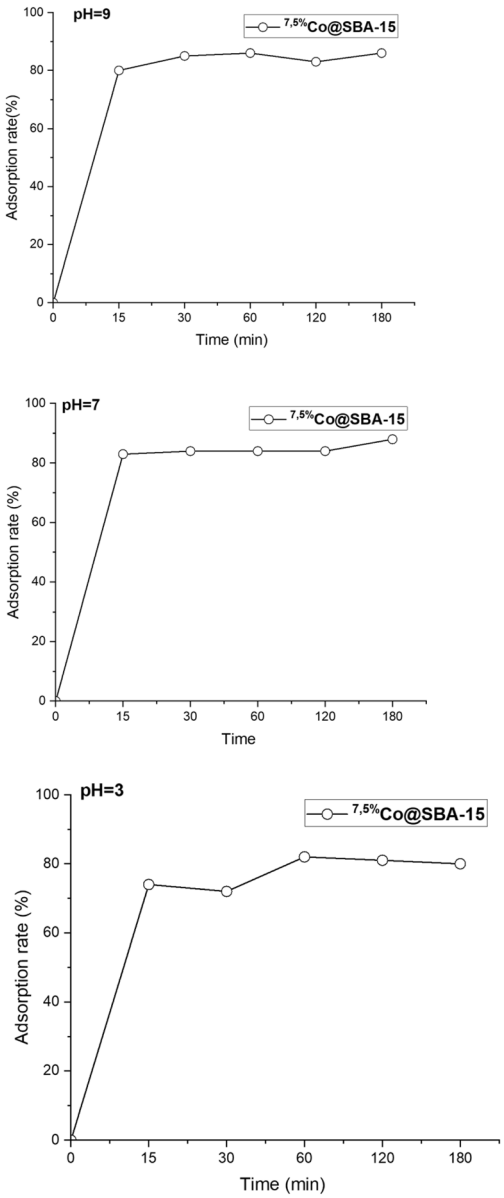

Fig. 10 Adsorption of tetracycline at different pH over $^{7.5\%}$Co@SBA-15.

of new signals at 1450, 1506, 1557, 1627 cm^{-1}, among others, attributed to the functional groups *ex*. C=C stretching, C–N, NH_2, C=O, and of tetracycline confirms its successful adsorption.[52,53]

We next attempted the material recycling using **$^{5\%}$Co@SBA-15** after successive regeneration. After each adsorption cycle, the adsorbent was recovered and thoroughly washed with distilled water and ethanol to remove pollutants. The material was then air-dried, followed by further drying in an oven at 80 °C for 2 h before reuse. Delightedly, tetracycline adsorption could be repeated several times, with a marginal decrease in the adsorption performance (Fig. 11). The recyclability reached herein is very promising considering that milder and eco-friendly conditions were applied herein for the material recovery and its regeneration.

Mechanistically, tetracycline removal generally proceeds through pore filling, hydrogen bonding, ion exchange, acid-base interactions, and π–π stacking. The latter is unlikely in the present system given the inorganic nature of the material and the absence of an aromatic, carbon-based framework. In contrast, pore filling is clearly plausible, as the molecular size of tetracycline is sufficiently small to be accommodated within the pores of the adsorbents without significant thermodynamic penalty.

The insensitivity of the adsorption performance to pH variations further suggests that ion exchange is not the dominant driving force for tetracycline-adsorbent interactions. Given the well-established relationship between surface acidity and adsorption performance as discuss above, the involvement of both acid-base coordination and hydrogen bonding interplay can be reasonably proposed. The facile regeneration of the adsorbent under mild conditions, using only water and ethanol, reflects the weak nature of the interfacial interactions, most plausibly through hydrogen bonding, whereas nitrogen-to-cobalt coordination would be expected to require harsher regeneration conditions. The suppression of tetracycline adsorption upon trimethylsilylation further supports this assumption, as trimethylsilylation consumes residual silanol groups and consequently reduces the surface's propensity for hydrogen bonding. In light of these observations, it is reasonable to assume the predominance of hydrogen-bonding sites, together with a smaller population of sites involved in base-to-acid coordination. These two types of adsorption sites are consistent with the Freundlich adsorption mechanism governing the process.

To further challenge the performance of **$^{7.5\%}$Co@SBA-15**, we next investigated the adsorption of tetracycline at greater concentrations of 10^{-3} M (Fig. S22 and S23). While an over saturation of the surface-adsorbing sites is expected at this concentration, the removal efficiency still high, reaching 69% after 3 hours.

To conduct additional elimination, we subjected such highly concentrated 10^{-3} mol L^{-1} tetracycline solution to visible light irradiation for seven hours in the presence of **$^{7.5\%}$Co@SBA-15**. We noticed a further decrease of tetracycline concentration to achieve 85% elimination (Fig. S23). This indicates that once reaching its equilibrium, the corresponding solid operates as a photo-catalyst to trigger oxidative scission of the pharmaceutical towards its mineralization (Fig. 12). Total organic carbon analysis of the photo-catalytically treated solution reveals a removal percentage of nearly 100% against 35% only for the one treated only by adsorption (Fig. S24), which unambiguously confirm that the process is truly operating by sequential adsorption and photo-oxidative degradation. These metal oxide-loaded **SBA-15** represent indeed a practical solution for the purification of wastewater containing discrete pharmaceutical pollutants, which are generally found at much lower concentrations (from a few nanograms per litre to micrograms per litre).[54]

Radical scavenging experiments were performed to elucidate the dominant reactive species responsible for the photocatalytic degradation of tetracycline (Fig. 12). The degradation efficiency in the absence of scavengers reached approximately 85%. A marginal decrease in degradation efficiency was observed (83%)

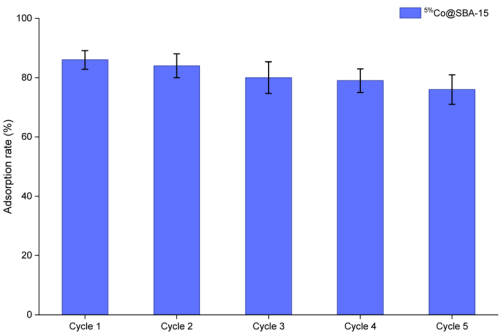

Fig. 11 Recycling experiments of the adsorption of tetracycline solution [C = 10^{-4} mol L^{-1}] using **$^{5\%}$Co@SBA-15**.

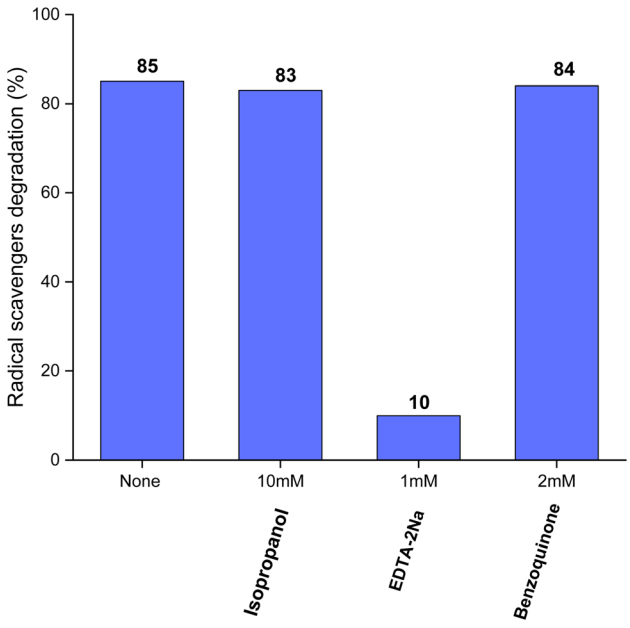

Fig. 12 Visible-light photocatalytic activity of **$^{7.5\%}$Co@SBA-15** against tetracycline (C = 10^{-3} mol L^{-1}) assuming an equilibrium of adsorption after 3 hours and the corresponding radical scavenging tests.

by adding 10 mM of isopropanol, a well-known hydroxyl radical ($^{\bullet}OH$) scavenger, indicating that $^{\bullet}OH$ radicals play a minor role in the photocatalytic process. Similarly, the use of benzoquinone (2 mM), a scavenger for superoxide radicals ($^{\bullet}O_2^-$), resulted in a negligible change (84%), suggesting a limited contribution of $^{\bullet}O_2^-$ species. In sharp contrast, the introduction of EDTA-2Na (1 mM), a selective scavenger for photogenerated holes (h^+), caused a dramatic suppression of tetracycline photodegradation efficiency to approximately 10%. This pronounced inhibition clearly demonstrates that photo-generated holes are the predominant reactive species governing the photocatalytic degradation in this system. The results indicate that the degradation pathway is mainly driven by direct oxidation of the pharmaceutical by holes or by hole-mediated surface reactions, rather than by hydroxyl or superoxide radicals. Overall, these findings provide strong mechanistic evidence that h^+ plays a decisive role in the photocatalytic degradation process.[55,56]

We next attempted $^{7.5\%}$**Co@SBA-15** recycling for the second and third run of adsorption and photocatalysis (Fig. 13). After the first cycle achieving 65% adsorption followed by 85% after visible-light irradiation, the solid adsorbent was recovered from the medium by filtration, immersed in a solution of sodium chloride salt (1 mol L^{-1}) for 30 minutes, and next filtered and air-dried for 1 hour at 80 °C prior to recycling. In the second run, significant reduction of the adsorption capacity was noticed as tetracycline uptake stabilized at 23%. The reason for this decrease could be tentatively attributed to the decrease in the specific surface are of the photocatalytic material, being equal to 100 m^{-2}. Such dramatic decrease is expected to substantially affect the adsorption performance of the photocatalyst. However, subjecting that medium to visible-light irradiation enables more tetracycline degradation, until 79% elimination. In the third cycle, the material seems to keep the same activity in both adsorption and photo-catalysis. Improving the framework stability during light irradiation could be the key for long-term use of the present water-cleaning systems.

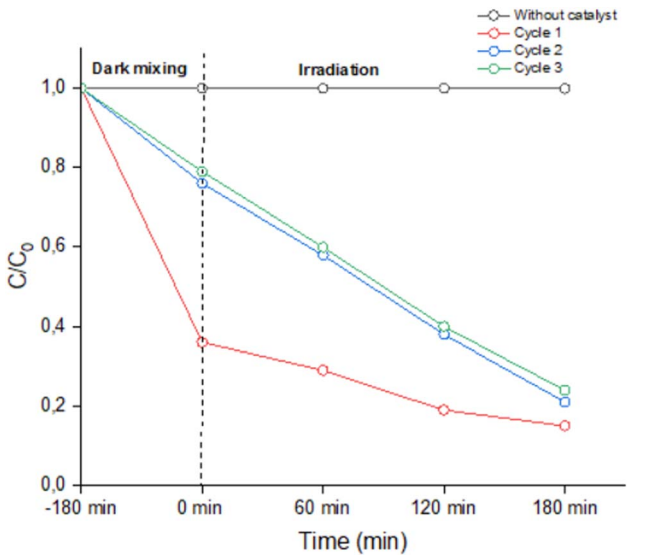

Fig. 13 Recycling photocatalytic experiments of tetracycline (C = 10^{-3} mol L^{-1}) degradation with $^{7.5\%}$**Co@SBA-15** assuming an adsorption equilibrium after 3 hours.

Conclusion

In conclusion, we herein report the successful design of mesostructured **SBA-15** based hybrid materials incorporating ultrasmall cobalt oxide clusters as dual-function systems for pharmaceutical remediation. The synergy between the high surface area of **SBA-15** and the semiconducting properties of confined Co_3O_4 clusters bridged through photoactivatable Si–O–Co interface enabled both efficient adsorption and visible-light-driven photocatalytic degradation of tetracycline, significantly outperforming conventional adsorbents and metal oxides (Tables S4 and S5). The critical role played by (i) residual pluronic during seeding and growth of the metal oxide clusters, (ii) thermal annealing in further fusing and stabilizing the hybrid structure and (iii) tuning surface polarity for maximizing the interaction with the pollutant; all of them highlight the importance of surface-interface engineering towards high-performance materials. These findings provide a sustainable solution to antibiotic contamination in aquatic environments and open new avenues for the development of multifunctional adsorbent-photocatalyst platforms tailored for emerging pollutants. Future efforts may focus on extending this strategy to other pharmaceutical residues, optimizing photonic properties, and processing into membrane for real wastewater treatment.

Author contributions

Hajar Tallouzt: investigation, formal analysis, data curation, writing – original draft. Céline Nayral: formal analysis, visualization, writing – review & editing. Jamal El Haskouri: formal analysis, writing – review & editing. Khalil Anis: supervision, writing – review & editing. Abdelhak Kherbeche: supervision, writing – review & editing, Abdelkrim El Kadib: conceptualization, methodology, visualization, validation, writing – original draft. Writing – review & editing.

Conflicts of interest

The authors declare no competing financial interest.

Data availability

The data supporting this article have been included as part of the supplementary information (SI). Supplementary information: characterizations including infrared, TGA, XRD, UV-vis, SEM images, HRTEM, XPS, N_2 adsorption–desorption, and NMR. See DOI: https://doi.org/10.1039/d5ra08136j.

Acknowledgements

UEMF is acknowledged for the financial support. The authors are grateful to Projet Toubkal PHC 23/173. Dr Ghanem Hamdoun (UEMF) is warmly acknowledged for solid-state NMR analyses.

References

1 Y. Zhou, J. Wang, J. Yang, L. H. Duan, H. B. Liu, J. Wu and L. Gao, *ACS Appl. Nano Mater.*, 2024, **7**, 3806–3816.
2 L. Ji, F. Liu, Z. Xu, S. Zheng and D. Zhu, *Environ. Sci. Technol.*, 2010, **44**, 3116–3122.
3 X. Liu, H. He, B. Zhao, L. Zhou, X. Zhao, C. Wang, J. Zhang, Y. Zhang and L. Wang, *Langmuir*, 2024, **40**, 16291–16302.
4 X. Liu, G. Zhang, Y. Liu, S. Lu, P. Qin, X. Guo, B. Bi, L. Wang, B. Xi, F. Wu, W. Wang and T. Zhang, *Environ. Pollut.*, 2019, **246**, 163–173.
5 M. Patel, R. Kumar, K. Kishor, T. Mlsna, C. U. Pittman and D. Mohan, *Chem. Rev.*, 2019, **119**, 3510–3673.
6 M. Noori Keshtkar, S. A. Mousavi and H. Molavi, *Langmuir*, 2025, **41**, 13395–13406.
7 Z. P. Zanele, F. M. Mtunzi, S. M. Nelana, A. N. Ebelegi, N. Ayawei, E. D. Dikio, D. Wankasi and P. N. Diagboya, *Langmuir*, 2021, **37**, 9764–9773.
8 J. Wang, F. Li, Y. Bao and S. Zhan, *Adv. Sustain. Syst.*, 2025, **9**, 2400634.
9 A. Balakrishnan, E. S. Kunnel, S. Trivedi, R. Sasidharan, A. Kumar and M. Chinthala, *Ind. Eng. Chem. Res.*, 2024, **63**, 18975–18988.
10 J. Yang, J. Wu, L. Gao, L. H. Duan and J. Wang, *New J. Chem.*, 2024, **48**, 19101–19112.
11 N. S. Sanjini and S. Velmathi, *RSC Adv.*, 2014, **4**, 15381–15388.
12 X. Yang, X. Li, Y. Hu, J. Cheng and Y. Chen, *Water*, 2022, **14**(6), 910.
13 Z. Fan, J. Fang, G. Zhang, L. Qin, Z. Fang and L. Jin, *ACS Omega*, 2022, **7**, 30543–30553.
14 J. Yang, J. Wu, L. Gao, L.-H. Duan and J. Wang, *New J. Chem.*, 2024, **48**, 19101.
15 Q. Li, Y. Zheng, L. Guo, Y. Xiao, H. Li, P. Yang, L. Xia, X. Liu, Z. Chen, L. Li and H. Zhang, *J. Agric. Food Chem.*, 2024, **72**, 13523–13536.
16 S. Al-Salihi, M. M. Fidalgo and Y. Xing, *ACS ES & T Water*, 2023, **3**, 838–847.
17 S. Hashemikia, N. Hemmatinejad, E. Ahmadi and M. Montazer, *J. Colloid Interface Sci.*, 2015, **443**, 105–114.
18 M. Ramírez-Hernández, B. Thomas, C. Tang, Z. Huang and T. Asefa, *Chemelectrochem*, 2021, **8**, 4296–4304.
19 Y. Yang, L. Chen, M. Li and X. Qiu, *Ind. Eng. Chem. Res.*, 2025, **64**, 6967.
20 M. Ferenc, N. Katir, K. Miłowska, M. Bousmina, J. P. Majoral, M. Bryszewska and A. El Kadib, *J. Mater. Chem. B*, 2015, **3**, 2714–2724.
21 J. Zhang, Z. Ma, J. Jiao, H. Yin, W. Yan, E. W. Hagaman, J. Yu and S. Dai, *Langmuir*, 2009, **25**, 12541–12549.
22 Y. Wan and D. Zhao, *Chem. Rev.*, 2007, **107**, 2821–2860.
23 M. El Kaddouri, D. Akmach, N. Katir, J. El Haskouri, S. Kaliaguine and A. El Kadib, *ChemCatChem*, 2025, **17**, e202500382.
24 N. S. Sanjini and S. Velmathi, *RSC Adv.*, 2014, **4**, 15381–15388.
25 J. H. Tsai, T. Y. Lee and H. L. Chiang, *Nanomaterials*, 2023, **13**, 1015.
26 M. Audemar, C. Ciotonea, K. De Oliveira Vigier, S. Royer, A. Ungureanu, B. Dragoi, E. Dumitriu and F. Jérôme, *ChemSusChem*, 2015, **8**, 1885–1891.
27 M. F. Kamaruzaman, Y. H. Taufiq-Yap and D. Derawi, *Biomass Bioenergy*, 2020, **134**, 105476.
28 D. Zhao, J. Feng, Q. Huo, N. Melosh, G. H. Fredrickson, B. F. Chmelka and G. D. Stucky, *Science*, 1998, **279**, 548–552.
29 C. F. Toncón-Leal, J. F. Múnera, J. J. Arroyo-Gómez and K. Sapag, *Catal. Today*, 2022, **394–396**, 150–160.
30 V. Chaudhary and S. Sharma, *J. Porous Mater.*, 2017, **24**, 741–749.
31 Y. Brahmi, N. Katir, J. A. M. I. Agullo, A. Primo, M. Bousmina, J. Pierre Majoral, H. Garcia and A. El Kadib, *Dalton Trans.*, 2015, **44**, 15544–15556.
32 E. Pędziwiatr-Werbicka, K. Miłowska, M. Podlas, M. Marcinkowska, M. Ferenc, Y. Brahmi, N. Katir, J. P. Majoral, A. Felczak, A. Boruszewska, K. Lisowska, M. Bryszewska and A. El Kadib, *Chem.—Eur. J.*, 2014, **20**, 9596–9606.
33 P. T. T. Thu, H. T. Dieu, H. N. Phi, N. N. T. Viet, S. J. Kim and V. Vo, *J. Porous Mater.*, 2012, **19**, 295–300.
34 T. Liu, T. Jiang, J. Zhu, T. Rui, S. Zheng and Z. Hu, *New J. Chem.*, 2023, **47**, 22125–22133.
35 Y. Brahmi, N. Katir, A. Castel and A. El Kadib, *Microporous Mesoporous Mater.*, 2013, **177**, 75–81.
36 Z. Liu, J. Niu, W. Long, B. Cui, K. Song, F. Dong and D. Xu, *Inorg. Chem.*, 2020, **59**, 7335–7343.
37 J. Jian, D. Kuang, X. Wang, H. Zhou, H. Gao, W. Sun, Z. Yuan, J. Zeng, K. You and H. Luo, *Mater. Chem. Phys.*, 2020, **246**, 122814.
38 S. Kalasina, K. Kongsawatvoragul, N. Phattharasupakun, P. Phattharaphuti and M. Sawangphruk, *RSC Adv.*, 2020, **10**, 14154–14160.
39 H. Saini, S. Vishwanathan, S. Sil, N. S. Kumar and H. S. S. R. Matte, *ACS Appl. Nano Mater.*, 2025, **8**, 917–923.
40 T. M. Lima, V. de Macedo, D. S. A. Silva, W. N. Castelblanco, C. A. Pereira, R. E. Roncolatto, M. B. Gawande, R. Zbořil, R. S. Varma and E. A. Urquieta-González, *Appl. Catal., B*, 2020, **277**, 119248.
41 Q. Q. Hao, Y. H. Zhao, H. H. Yang, Z. T. Liu and Z. W. Liu, *Energy Fuels*, 2012, **26**, 6567–6575.
42 S. T. Pham, M. B. Nguyen, G. H. Le, T. T. T. Pham, T. T. T. Quan, T. D. Nguyen, T. Le Son and T. A. Vu, *J. Chem.*, 2019, **2019**, 5785621.
43 H. M. Salem, R. S. Mohamed, A. A. Alkahlawy, H. M. Gobara, A. E. A. Hassan and S. A. Hassan, *J. Porous Mater.*, 2019, **26**, 735–745.
44 J. D. Jimenez, C. Wen, M. M. Royko, A. J. Kropf, C. Segre and J. Lauterbach, *ChemCatChem*, 2020, **12**, 846–854.
45 H. J. Khan, J. Ding, J. Qu, G. V. Sarrigani, P. Fitzgerald, X. Xu, A. E. Ghadi, Q. Sui, C. Tian, J. M. Cairney, D. Wiley and D. Wang, *Appl. Catal., A*, 2025, **706**, 120469.
46 J. Gao, X. Zhang, Y. Yang, J. Ke, X. Li, Y. Zhang, F. Tan, J. Chen and X. Quan, *Chem.–Asian J.*, 2013, **8**, 934–938.

47 K. Bakkouche, A. Anouar, N. Katir, C. Nayral, F. Delpech and A. El Kadib, *FlatChem*, 2023, **39**, 100502.
48 T. X. Bui and H. Choi, *J. Hazard. Mater.*, 2009, **168**, 602–608.
49 I. Langmuir, *J. Am. Chem. Soc.*, 1919, **40**, 1361–1403.
50 A. Proctor and J. F. Toro-Vazquez, *Bleaching and Purifying Fats and Oils: Theory and Practice*, 2009, vol. 73, pp. 209–219.
51 Z. Zhang, H. Liu, L. Wu, H. Lan and J. Qu, *Chemosphere*, 2015, **138**, 625–632.
52 M. Ghadiri, H. Hau, W. Chrzanowski, H. Agus and R. Rohanizadeh, *RSC Adv.*, 2013, **3**, 20193–20201.
53 F. Fookes, S. Bongiovanni Abel, J. F. Martucci, D. Estenoz, G. A. Abraham and C. A. Busatto, *Pharmaceutics*, 2025, **17**, 1335.
54 S. Boonyuen, S. M. Smith, A. Luengnaruemitchai, P. N. Nakorn, Y. Tangjaideborisu and P. Shanmugam, *Inorg. Chem. Commun.*, 2025, **173**, 113862.
55 J. Ding, H. J. Khan, G. Vahedi Sarrigani, P. Fitzgerald, A. Ebrahimi Ghadi, O. Lefebvre, C. Meng, M. H. Z. Mohd Harun, Y. Lu, A. Abbas, A. Montoya, D. Wiley and D. K. Wang, *Chem. Eng. J.*, 2022, **432**, 134435.
56 H. J. Khan, J. Ding, J. Qu, G. V. Sarrigani, P. Fitzgerald, X. Xu, A. E. Ghadi, Q. Sui, C. Tian, J. M. Cairney, D. Wiley and D. Wang, *Appl. Catal., A*, 2025, **706**, 120469.